Control of vortex shedding in an axisymmetric bluff body wake

Ansgar Weickgenannt [a], Peter A. Monkewitz [b,*]

[a] *ABB Turbosystems AG, CH-5400 Baden, Switzerland*
[b] *Ecole Polytechnique Fédérale de Lausanne, Laboratoire de Mécanique des Fluides, CH-1015 Lausanne EPFL, Switzerland*

Abstract – In the present experimental study the effect of a control disc mounted at the rear of an axisymmetric blunt-based body of revolution, first studied by Mair, is investigated in the Reynolds number range $3 \times 10^3 \leqslant Re_D \leqslant 5 \times 10^4$. As the distance of the control disc from the blunt base is increased, four vortex shedding regimes are identified: at small distances there is no effect, then a sharp increase of vortex shedding activity and total drag is observed, followed by an interval with reduced activity and drag and finally at large distances a regime where the flow around the main body and disc become essentially independent, i.e. where the drag forces of the two elements become additive. The near and far wake velocity fields corresponding to the different regimes are documented with time- and phase-averaged hot-wire and LDA measurements, with spectral analysis of the data and with flow visualizations of the near wake. The results are used to develop an improved understanding of the instability mechanism leading to high vortex shedding activity. © 2000 Éditions scientifiques et médicales Elsevier SAS

1. Introduction

The control of vortex shedding behind bluff bodies is a subject of continued high interest and considerable practical importance. Most efforts have so far been concentrated on suppressing vortex shedding from bluff bodies (among many studies, see, e.g., Roshko [1,2], Monkewitz [3], Schumm et al. [4], Roussopoulos and Monkewitz [5] and references therein) in order to reduce drag of vehicles, for instance, flow induced vibrations, noise, etc. The increase of vortex shedding, on the other hand, has received comparatively little attention despite its obvious interest for increasing the fluid entrainment into a wake. The control of entrainment can in turn be used to control the mixing rate between different fluids or reactants. This connection between entrainment by large-scale structures and mixing has been studied extensively in the plane mixing layer by Koochesfahani and Dimotakis [6], for instance. They found, in short, that fluid from both sides of the mixing layer is rolled into the large-scale vortical structures, thereby increasing the interface area across which molecular mixing between two species, i.e. diffusive transport can take place. Hence, increased entrainment generally leads to an increased mixing or reaction rate.

Large-scale structures in axisymmetric wakes have been studied for different wake-generating bodies such as spheres (Achenbach [7], Taneda [8]), disc's (Scholz [9], Berger et al. [10]) and more general bodies of revolution (Schwarz [11], Fuchs [12]), to name just a few, and the dominant structure has been found to be either a single vortex spiral or a pair of counter-rotating spirals, corresponding to a flapping of the wake in a fixed plane. In the present study we focus on the wake of an axisymmetric 'cigar-shaped' body with the blunt end facing downstream, which has first been investigated by Mair [13] (see *figure 1*). Motivated by the problem of reducing the drag of motor vehicles, he investigated in particular the effect of a rear-mounted disc on the drag and the base pressure of such a body at $Re_D = 1.47 \times 10^5$, where the Reynolds number is based

---

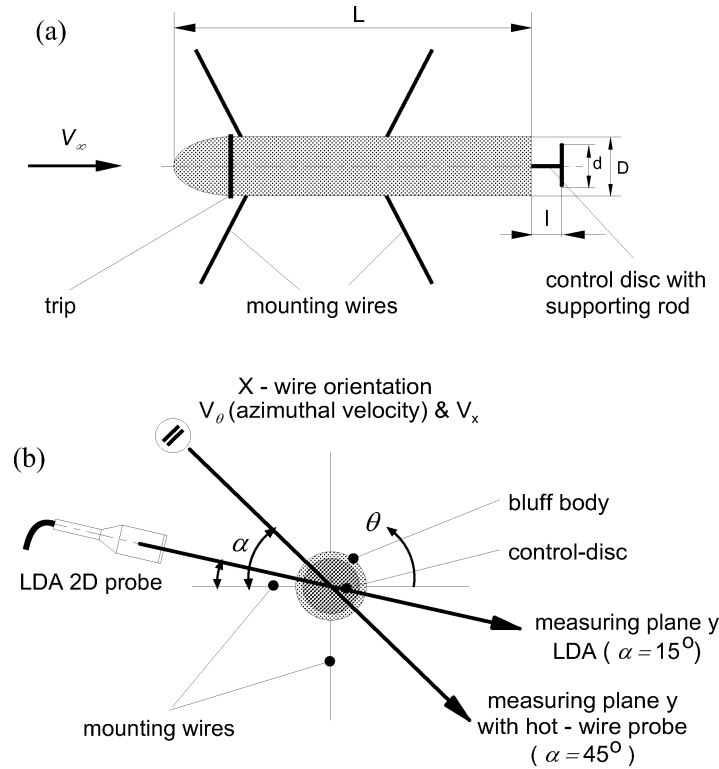* Correspondence and reprints; e-mail: peter.monkewitz@epfl.ch

Figure 1. Sketch of the Mair-body and coordinate system; (a) side view; (b) back view with definition of probe traversing directions.

on the diameter D of the cylindrical part of the main body and the freestream velocity V_∞. The configuration of *figure 1* with a rear-mounted disc will hence be denoted as a Mair-body throughout this study. Mair found that the drag of the entire model, measured with an aerodynamic balance, was strongly affected by the distance l between the control disc and the base of the cylinder when the control disc diameter d and other geometrical parameters were optimized for maximum drag reduction. With his optimal ratio of control disc to cylinder diameter $d/D = 0.8$, which will also be used in the present study, Mair identified three drag regimes (his results are displayed later in *figure 3*): for small disc distances l/D he found no effect on drag because the mixing layer leaving the trailing edge of the cylinder stays well clear of the disc edge (his figure 13a, discussed here in section 4.2). For $l/D \approx 0.3$, Mair discovered an unexpected, highly unsteady regime with a total drag increase of up to 120 %. He speculated that the increase was due to a large amplitude flapping motion of the mixing layer, leading to its periodic impingement on the upstream face of the disc, but did not investigate this regime further. Finally, for still larger l/D, Mair found a relatively steady regime with drag reduced by as much as 30 % relative to the configuration without a disc. He explained this phenomenon by the low pressure associated with a strong vortex ring "locked" in the cavity between cylinder base and disc, which draws in the mixing layer and leads to an improved pressure recovery at the rear of the body and hence to a pressure increase on the downstream face of the disc (his figure 13b, discussed here in section 4.2).

Mair's work was taken up by Little and Whipkey [14] who used a geometry similar to Mair's for their investigation. With a smaller disc of $d/D = 0.75$ they obtained an analogous relation between drag and disc spacing l at $Re_D = 1 \times 10^5$, which was however shifted towards larger l. Furthermore, using LDA they were the first to document the time-mean of the flow inside the cavity for different disc positions. For small disc distances before the drag increase, they did identify a counter-rotating vortex ring in the cavity between base

and disc, i.e. a ring with azimuthal vorticity opposite to the vorticity of the surrounding shear layer, and a reverse flow over the disc edge into the cavity. At control disc positions l corresponding to low drag, on the other hand, a co-rotating vortex was found in the cavity. They did not, however, investigate the high drag regime where the flow is highly unsteady.

It was primarily this unexpected and unexplained high drag regime which independently caught the attention of Fernholz (Fiedler and Fernholz [15]) and Monkewitz in the late eighties and led to the preliminary study of Monkewitz and Fernholz [16] (see also Fernholz [17]) who studied the wake dynamics as a function of the disc spacing l. Their investigation was carried out in the laminar wind tunnel of the Hermann-Föttinger Institute in Berlin, which has a circular cross section of 441 mm diameter, with a Mair-body of $D = 2$ in. and $Re_D = 2.4 \times 10^4$. The high quality of the Berlin tunnel permitted them to relate quantitatively the increase of total drag to an increase of vortex shedding activity as l was decreased through the transition from low to high drag. The velocity spectra in the wake, in particular, and the dependence of a characteristic perturbation amplitude on the control parameter l strongly supported the view that the transition from low to high drag is a Hopf bifurcation to self-excited spiral vortex shedding, analogous to the Hopf bifurcation leading to Kármán shedding behind a cylinder, first identified by Provansal et al. [18]. The spiral nature of the shedding in the high drag regime of the Mair-body was established by the observation of Monkewitz and Fernholz that the phase of cross-spectra between diametrically opposite sides of the wake was always π at the fundamental shedding frequency.

The above preliminary work did however still not explain the mechanism leading to the high drag regime and it is the main purpose of the present paper to elucidate this mechanism. First, the effect of different parameters, such as Re_D and the state of the boundary layer at the trailing edge of the cylinder, on the drag variation and the mean wake profiles are investigated in sections 3.1 and 3.2, which complement the studies of Mair [13] and Little and Whipkey [14]. Then, the relation between vortex shedding activity and drag is established in section 3.3. This leads to the central section 4 of the paper in which detailed measurements of the flow field around the control disc and in the near wake are used to analyze, in terms of linear stability boundaries, the transition to the high drag regime coming both from low l/D values (where no effect on drag is observed) and from high values (where drag is reduced).

2. Experimental setup

The experiments were performed in an open loop wind tunnel with a rectangular test section of 300×445 mm, located at EPFL's fluid mechanics laboratory (for a detailed description see Weickgenannt [19]). The tunnel has been specially designed for carrying out sensitive experiments on flow instabilities, with a low turbulence level of 0.15%, no pronounced spectral components, and a flow uniformity better than 1% of the mean.

The model in the present study corresponds to the configuration with which Mair [13] found the largest drag reduction. It had a diameter D of 30 mm and a total length to diameter ratio of $L/D = 6$ (*figure 1(a)*). The nose of the Mair-body was rounded over the first 25 mm of length at which point a fence of 250 μm height was permanently mounted for boundary layer tripping. The control disc at the rear of the cylinder had a diameter of $d = 0.8 \, D$ and a thickness of 0.041 D with a semi-circular edge. It was mounted to the rear of the cylinder with a rod of 4 mm diameter. The distance l between the base of the main body and the control disc, which is one of the main control parameters in our study, will henceforth be specified in the following non-dimensional form:

$$s = \frac{l}{D}. \tag{1}$$

The model was suspended in the wind tunnel test section by two sets of four tungsten wires of 120 μm diameter, one set near the nose and the second set at 2/3 of the length of the model. All wires were aligned in the vertical and horizontal planes, respectively, such that the downstream set was in the wake of the four front support wires (see *figure 1*). This choice was found to be the best compromise between wire strength, stiffness and flow perturbation. The axis of the Mair-body was aligned parallel to the free stream to within $\pm 0.5°$. This accuracy was necessary since a misalignment of more than $1°$ leads to a detectable asymmetry of the mean axial velocity profile in the wake. The absence of model vibrations, finally, was verified visually with a telescope.

In the following, a cylindrical coordinate system $(x/D, r/D, \theta)$ with its origin at the center of the blunt base of the cylinder will be used, where all lengths are non-dimensionalized with D. The hot-wire probe and the probe volume of the LDA were traversed through the wake along a diameter inclined at an angle α with respect to the horizontal (refer to *figure 1(b)*) in order to avoid the wakes of the support wires. To simplify the presentation of data, the coordinate y/D along these diameters is introduced as follows:

$$\theta = \pi - \alpha \longrightarrow y/D = -r/D < 0,$$
$$\theta = 2\pi - \alpha \longrightarrow y/D = r/D \geqslant 0. \tag{2}$$

Measurements of the flow field were carried out with hot-wires and LDA. Both a single wire (Dantec model 55P01 with 5 μm wire) and an x-wire probe (designed by the Hermann-Föttinger Institute with 2.5 μm wires and a probe volume of about 0.35 mm cubed) have been used with a TSI IFA-100 constant temperature anemometer. The LDA was a two-component Dantec Fiberflow instrument with burst spectrum analyzers. The probe volume diameter was in most cases 146 μm with a length of 2.4 mm (for some measurements different optics had to be used with a probe volume of 190 μm $\times$ 4 mm). The LDA probe volume was traversed along the line shown in *figure 1(b)* ($\alpha = 15°$) to obtain the axial and azimuthal velocity components and normal to this line ($\alpha = 105°$) for the axial and radial components. In addition, flow visualizations using streamers made of single carbon fibers were carried out in the near wake.

3. Experimental results

3.1. The effect of the control disc position s on the mean wake profiles and drag – the four drag regimes

The effect of the control disc position $s = l/D$ on the mean axial velocity profile at $x/D = 4$ is shown in *figure 2* for $Re_D = 3.6 \times 10^4$ where the boundary layer leaving the trailing edge of the cylinder is fully turbulent (Reynolds number based on momentum thickness $Re_{\delta 2} = 567$; cf. section 3.2). For discussion later the associated power spectra measured at $x/D = 2.6$ and $r/D = 0.45$ are included on the same figure.

As the disc position is increased from $s = 0$ (solid thin lines on *figure 2*) to $s = 0.25$ (open squares), essentially no change of the wake profile is observed. At $s = 0.3$ however, the appearance of the mean profile is completely different: the width of the wake is considerably increased and the velocity deficit is much reduced. This profile is characterized by a local maximum of $V_x = 0.96$ on the centerline and a minimum, $V_x = 0.935$ at $r/D = 0.65$, leading to a distinct 'W-shape' of the profile. A further increase of s causes the width of the wake to decrease again and the local maximum on the axis to disappear, which amounts to a transition from a 'W-shaped' back to a standard wake profile. At the highest, $s = 0.48$ of *figure 2*, the shape of the standard wake profile is completely recovered, with the difference that this profile is slightly narrower than the profile for $s = 0$.
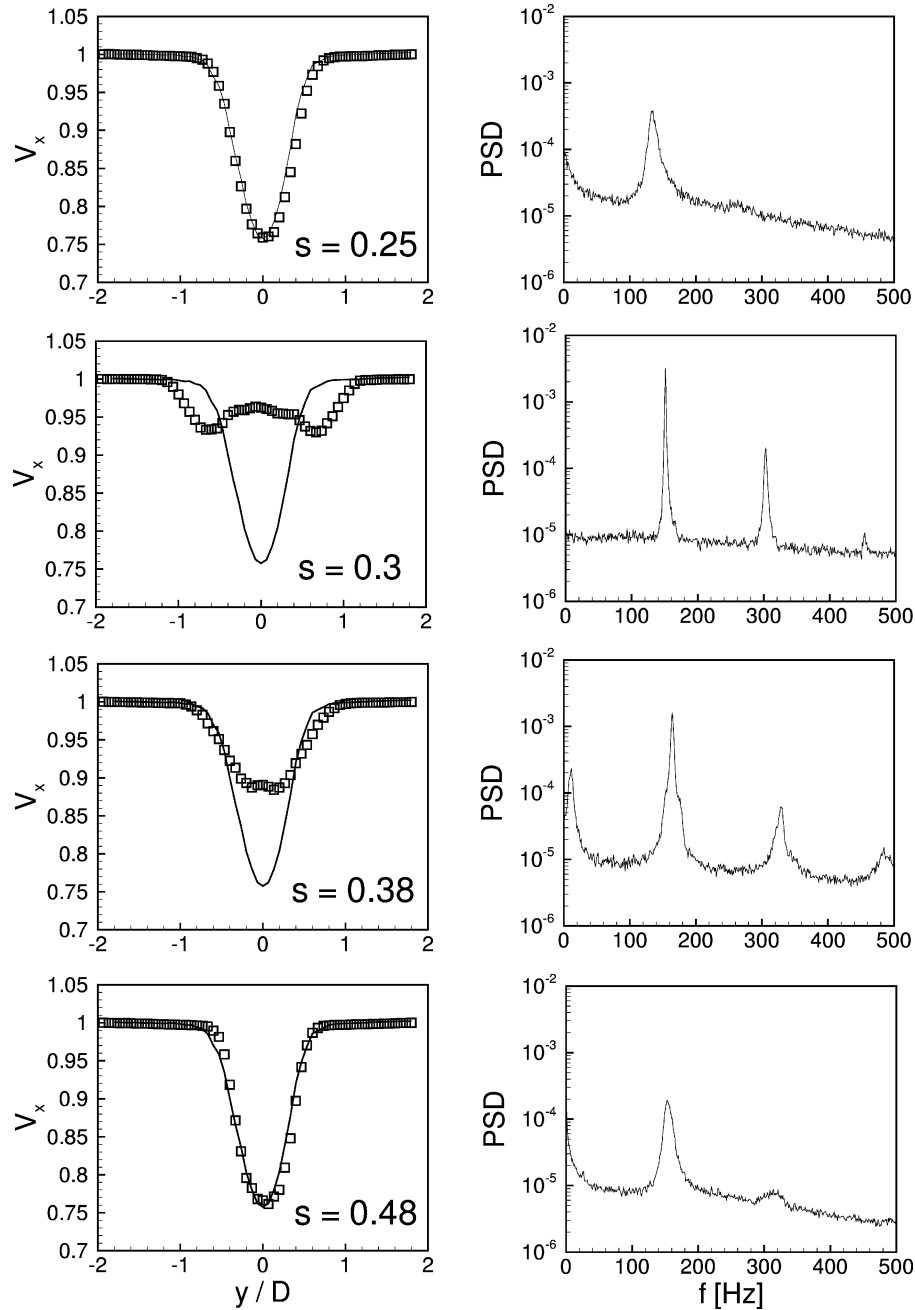
Figure 2. Left column: mean axial velocity profiles at $x/D = 4$ for fixed $Re_D = 3.6 \times 10^4$ and different control disc positions s (thin line: velocity profile without control disc). Right column: associated power spectral density (PSD) of the streamwise velocity perturbation, normalized by V_∞, at $x/D = 2.6$ and $r/D = 0.45$.

In summary, for intermediate values of control disc distance $s = 0.3, \ldots, 0.38$ we find qualitatively different axial velocity profiles corresponding to a wider, shallower wake with a characteristic local maximum on the axis. It is also noted that the power spectra, included on figure *figure 2* for discussion later, undergo a parallel evolution with a sharp increase of the fundamental amplitude and the appearance of higher harmonics

associated with the 'W-shaped' mean profiles. At lower Reynolds numbers, a similar evolution of the wake profiles and spectra with s is observed down to $Re_D = 2 \times 10^4$. Below this value, however, no 'W-shaped' profiles were found.

In order to relate the present results to Mair's [13] drag measurements obtained with an aerodynamic balance, we estimate the total drag of the cylinder plus control disc from the mean axial velocity profiles by the momentum integral method. Provided the contribution of pressure forces is negligible (Weickgenannt [19] has shown that this assumption is valid if the downstream control surface is placed at $x/D \geqslant 4$), the total drag force is obtained from the integral form of the momentum and continuity equations as:

$$F_x = \rho \int_{r=0}^{\infty} \int_0^{2\pi} V_x(r)\big[V_\infty - V_x(r)\big] r \, \mathrm{d}r \, \mathrm{d}\theta, \tag{3}$$

and the corresponding drag coefficient is:

$$c_D = \frac{F_x}{\frac{\rho}{2} V_\infty^2 \frac{\pi}{4} D^2}. \tag{4}$$

The r-integral in equation (3) is evaluated with the trapezoidal approximation on a domain extending to $r_{\max}$, where $V_x(r_{\max})/V_\infty = 0.99$. The θ-integration, on the other hand, was approximated by the arithmetic mean of the two half-profiles for $y < 0$ and $y > 0$.

To establish a reference, the drag coefficient of the Mair-body without control disc $c_D(s = 0)$ has been estimated for different Reynolds numbers and is listed in *table I*.

The drag as a function of control disc position s for different Reynolds numbers, estimated from the mean axial velocity profiles is now displayed in *figure 3* as a deviation from the baseline case, i.e. $\Delta c_D = c_D(s) - c_D(s = 0)$. For comparison, Mair's result for his 'short' body is also included on this figure.

At the lowest Reynolds number $Re_D = 8.8 \times 10^3$, *figure 3* shows no effect of s on drag, i.e. $\Delta c_D \approx 0$ in the s-interval of interest. At all larger Reynolds numbers, on the other hand, one can identify four distinct regimes in the $\Delta c_D - s$ relationship that are readily correlated with the variation of the mean wake profiles of *figure 2*:

No effect regime 'No': for $0 \leqslant s < s_{No-Hi}$ the total drag and the mean axial velocity profiles in the wake remain essentially the same as for the Mair-body without control disc;

High drag regime 'Hi': in this second interval $s_{No-Hi} < s < s_{Hi-Lo}$ the total drag is significantly increased and the wake profiles take on the characteristic 'W-shape' shown in *figure 2*;

Low drag regime 'Lo': the high drag regime is followed by an interval $s_{Hi-Lo} < s < s_{Lo-T}$ in which the control disc causes a net drag reduction with respect to the Mair-body without control disc. At the same time the wake profiles revert to their standard shape but with a slightly smaller width than in the regime 'No'.

Tandem regime 'T': for larger separations $s > s_{Lo-T}$ the total drag once again increases as the cylinder and the disc start to act more and more like two individual bluff bodies in tandem.

Table I. Drag coefficient c_D ($s = 0$) for the Mair-body without control disc at different Reynolds numbers Re_D.

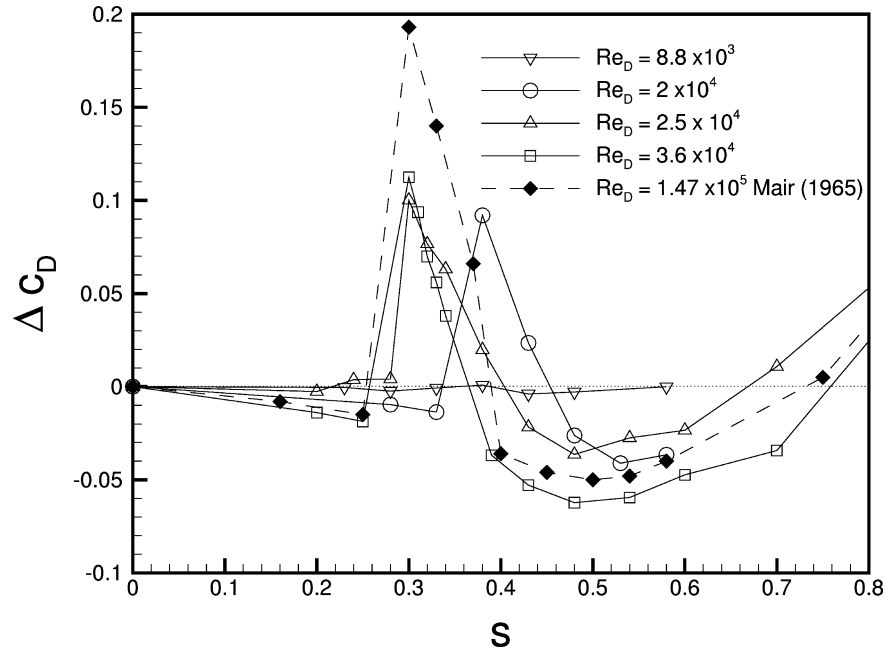| Re_D	8.8×10^3	2×10^4	2.5×10^4	3.6×10^4
c_D ($s = 0$)	0.22	0.268	0.276	0.297

Figure 3. Estimated drag differential Δc_D of the Mair-body versus control disc position s at $Re_D = 8.8 \times 10^3$, 2×10^4, 2.5×10^4, and 3.6×10^4 (open symbols). Result for $Re_D = 1.47 \times 10^5$ (solid symbol) adapted from Mair [13].

Table II. Dependence of maximum-drag control disc position s_{max} on Re_D.

Re_D	8.8×10^3	2×10^4	2.5×10^4	3.6×10^4	1.47×10^5 (Mair)
s_{max}	–	≈ 0.38	≈ 0.3	≈ 0.3	≈ 0.3

The evolution of these four regimes with Reynolds number appears clearly in *figure 3*: at Mair's Re_D and our largest $Re_D = 3.6 \times 10^4$ the s-intervals for the different regimes are virtually identical, which leads to the conclusion that the flow phenomena caused by the control disc are largely unaffected by viscous effects for $Re_D \geqslant 3.6 \times 10^4$. The only difference beween these two drag curves is the higher maximum drag at $s \approx 0.3$ obtained by Mair, which may well be due to the different measurement method (balance versus momentum integral). The maximum drag reduction at $s \approx 0.5$, on the other hand, is sensibly the same at the two highest Re_D of figure *figure 3*. This is consistent with Mair's finding that the drag reduction is approximately independent of Re_D.

As Re_D is lowered below 3.6×10^4, a progressive shift of the boundaries s_{No-Hi} and s_{Hi-Lo} towards higher s-values is observed, combined with a reduction of the low drag region, until both 'Hi' and 'Lo' regimes disappear below $Re_D = 1.8 \times 10^4$ (see Weickgenannt [19]). This trend is well characterized by the Reynolds number dependence of the control disc position s_{max}, given in *table II*, for which the drag of the Mair-body reaches its first maximum in the regime 'Hi'.

3.2. The connection between the occurrence of drag variations with s and the state of the boundary layer at the trailing edge of the cylinder

In the original high Reynolds number experiments of Mair [13] and Little and Whipkey [14], carried out at $Re_D = 1.47 \times 10^5$ and $Re_D = 1 \times 10^5$ respectively, the boundary layer at the trailing edge of the model was

Table III. Boundary layer parameters near the trailing edge
of the cylinder at $x/D = -0.16$ as a function of Re_D.

Re_D	$\leqslant 1 \times 10^4$	2.0×10^4	3.1×10^4
δ_2 [mm]	$48.1 \times Re_D^{-1/2}$	0.46	0.48
δ_ω [mm]	$218 \times Re_D^{-1/2}$	0.46	0.31
$Re_{\delta 2}$	$1.60 \times Re_D^{+1/2}$	3.1×10^2	5.0×10^2
H_{12}	$2.59 - 2.51$	1.63	1.42

Table IV. Dependence of the location x_s/D of the free stagnation point on
Re_D for $s = 0$.

Re_D	1×10^4	1.5×10^4	1.8×10^4	2×10^4	$\geqslant 2.3 \times 10^4$
x_s/D	1.76	1.50	1.24	1.18	≈ 1.1

clearly turbulent. It will turn out that the maximum radial velocity gradient, i.e. the vorticity thickness defined by $\delta_\omega = V_\infty/(\partial V_x/\partial r)_{\max}$ in the mixing layer surrounding the cavity between cylinder base and control disc is an important parameter for the vortex shedding phenomena to be studied. Since our Reynolds numbers are an order of magnitude lower than in Mair's study and the initial vorticity thickness of the mixing layer is directly related to the boundary layer profile (in particular its wall gradient) at the trailing edge of the cylinder, the latter was measured with a single hot-wire upstream of the trailing edge of the cylinder at $x/D = -0.16$ (without control disc).

It was found that, up to $Re_D = 1 \times 10^4$, the boundary layer near the trailing edge of the cylinder remains laminar with a Blasius profile corresponding to a distance from the leading edge equal to the distance from the tip of the Mair-body (cf. Weickgenannt [19]). In the interval $1 \times 10^4 < Re_D < 3 \times 10^4$ the trailing edge boundary layer is transitional and reaches a fully turbulent state at $Re_D = 3 \times 10^4$. The Reynolds number dependence of the measured boundary layer momentum thickness δ_2, $Re_{\delta 2}$, the corresponding vorticity thickness δ_ω based on the velocity gradient at the wall and the shape factor H_{12} are given in *table III*.

The parameters of *table III* are consistent with the observed state of the boundary layer, as $Re_{\delta 2}$ only exceeds the lower limiting value of $Re_{\delta 2} \approx 350$ for a turbulent boundary layer, given for instance by Fernholz and Finley [20], for $Re_D > 2 \times 10^4$. This also explains the ineffectiveness of the trip fence near the nose for $Re_D < 2 \times 10^4$ or, equivalently, for $Re_L < 1.2 \times 10^5$.

These observations strongly suggest that the high and low drag regimes can only appear in the present geometry if the boundary layer at the trailing edge of the cylinder is in an advanced transitional state or fully turbulent. As suggested above, we believe that it is primarily the reduced initial vorticity thickness δ_ω of the mixing layer leaving the trailing edge of the cylinder, which is important to obtain the dramatic effect of the control disc on the drag. In our geometry, the condition on the initial vorticity thickness necessary to obtain the high and low drag regimes is estimated to be $\delta_\omega \lesssim 0.5$ mm.

Another clue as to the relevant parameters for the observed drag variations, besides the initial vorticity thickness, is obtained from the length of the recirculation zone, which was determined by LDA in our setup without control disc and is presented in *table IV*.

The length of the recirculation zone, which is a measure of the streamwise curvature of the shear layer leaving the trailing edge of the cylinder as well as of the base pressure, is seen to decrease strongly up to

$Re_D \approx 2 \times 10^4$ and to remain approximately constant thereafter. [1] Significantly, this levelling off occurs at the Re_D below which no 'Hi' drag regime is observed for any disc position. This is also the Re_D at which the boundary layer at the cylinder trailing edge approaches a fully turbulent state leading to an increase of shear layer entrainment by as much as 30 % relative to laminar initial conditions (see for instance Dimotakis [22]). It is therefore reasonable to suspect that a minimum shear layer entrainment rate, or equivalently a minimum level of negative pressure in the cavity between cylinder base and control disc, are essential ingredients in the mechanism causing the 'Hi' drag regime.

3.3. The correlation between drag variation and vortex shedding activity

In the following, the vortex shedding in the wake of the Mair-body is related to the drag variations discussed in section 3.1. A first indication of the nature of this relation is obtained from the spectra of *figure 2*: the power spectrum in the regime 'No' at $s = 0.25$ has one rather low and broad peak at $f_0 = 133$ Hz ($St_D \equiv f_0 D / V_\infty = 0.21$), much like spectra due to a convective instability excited by external noise (see, e.g., Monkewitz [23]). As the boundary s_{No-Hi} is crossed, the dominant peak in the spectrum becomes narrower and higher (about a tenfold increase from $s = 0.25$ to $s = 0.3$). It is also shifted to a higher frequency $f_0 = 152$ Hz ($St_D = 0.24$) and the higher harmonics clearly emerge from the noise. This spectrum strongly suggests a limit cycle behaviour of the flow in the regime 'Hi', which becomes weaker as the boundary $s_{Hi-Lo} \approx 0.38$ is approached, i.e. the peak amplitude is reduced, the peaks broaden again and the harmonics become less pronounced, while the fundamental frequency remains approximately constant at f_0 ($s = 0.38$) = 162 Hz ($St_D = 0.26$). Finally, in the 'Lo' regime the spectrum again takes on the same appearance as in the 'No' regime, except that all levels are reduced by about half a decade and the fundamental frequency f_0 ($s = 0.48$) = 155 Hz ($St_D = 0.245$) remains at its 'Hi'-value.

To better pinpoint the different transitions in the $(Re_D - s)$ parameter space, the Strouhal–Reynolds relationship and the evolution of the dominant power spectral peak with Re_D are documented in *figure 4* for selected control disc positions s.

The $St_D - Re_D$ relations all collapse onto a single curve as long as the boundary layer at the trailing edge of the cylinder is laminar, i.e. up to $Re_D = 1 \times 10^4$ (see section 3.2). *Figure 4(b)* shows that in this laminar 'No'-regime a relatively weak vortex shedding activity exists. [2] As the trailing edge boundary layer becomes transitional, both Strouhal number and vortex shedding amplitude first drop. Then the curves of *figure 4* split into three distinct groups: for $s = 0.28$ the amplitude stays low and the Strouhal number reaches the constant value $St_D = 0.21$. From the previous discussion it is clear that for this disc position the system remains in the 'No'-regime for all Re_D investigated. At the largest $s = 0.5$ both St_D and amplitude vary smoothly through the transition region and, beyond $Re_D = 2.5 \times 10^4$, they take on constant values of $St_D = 0.24$ and PSD $= 2 \times 10^{-4} \approx 0$, similar to the PSD-values without control disc. The third group of curves for $0.3 \leqslant s \leqslant 0.42$, finally, shows a completely different behaviour with a simultaneous sharp rise of Strouhal number and PSD peak height (already noted by Little and Whipkey [14]) which permits us to clearly pinpoint the Reynolds number $Re_{D,No-Hi}$ for the 'No-Hi' transition. The decrease of $Re_{D,No-Hi}$ with increasing s is thereby fully consistent with the observed shift of the 'Hi'-regime towards higher values of s as Re_D is lowered (see *figure 3*). Beyond $Re_{D,No-Hi}$ the system remains in the 'Hi'-regime for this third group, except for $s = 0.42$ and $s = 0.38$ where transitions to the 'Lo'-regime, characterized by decreasing amplitudes, are observed. The Strouhal numbers,

---

[1] Note that this constant value is consistent with the result of $x_s/D = 1.05$ obtained by Porteiro at al. [21] for a similar geometry at $Re_D = 7.3 \times 10^4$.

[2] Note that the PSD's shown here are only indicative of the vortex shedding strength as they are all measured at the same fixed location which does in most cases not correspond to the location of maximum PSD.
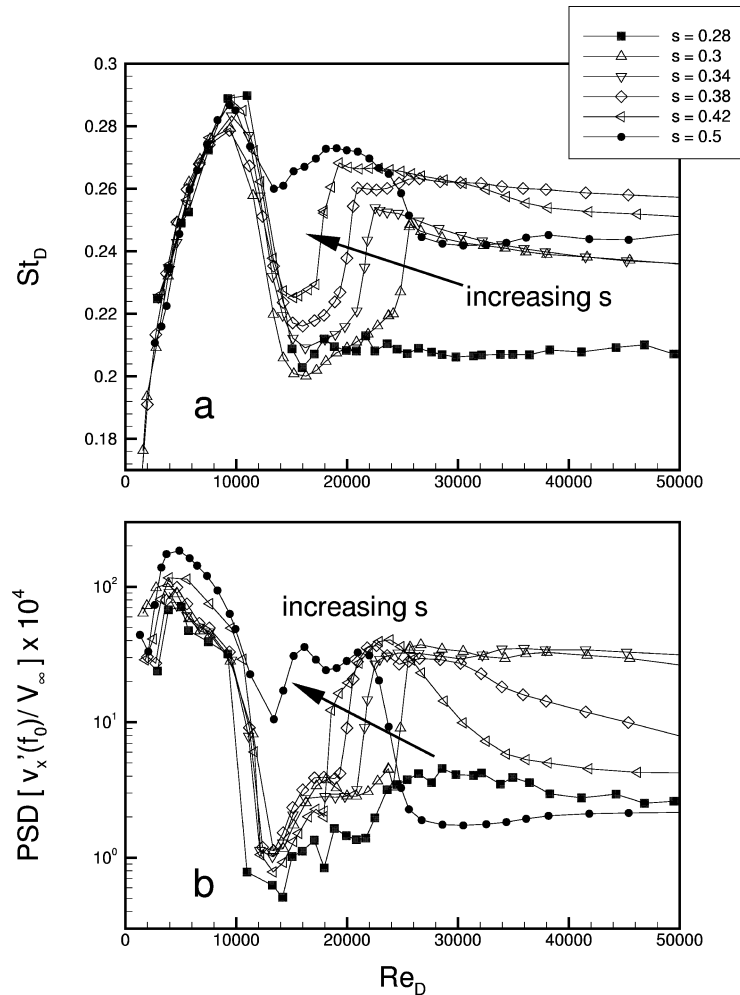
Figure 4. Strouhal number (a) and magnitude of peak power spectral density (b) of the longitudinal velocity fluctuations at the fundamental frequency f_0 measured at $x/D = 2.6$ and $r/D = 0.45$ versus Re_D for different control disc positions s (PSD's are multiplied by 10^4 to facilitate comparison with *figure 6*).

however, remain approximately constant beyond $Re_{D,No-Hi}$ and we note that in the cases where the system remains in the 'Hi'-regime ($s = 0.3$ and 0.34), the value of $St_D \approx 0.24$ reached at $Re_D = 5 \times 10^4$ is the same as Mair [13] found in his study for $s = 0.3$.

At this point we have to emphasize that the relationships shown on *figure 4* were all obtained from experimental runs in which Re_D was slowly increased. Runs with decreasing Re_D readily reveal that the abrupt 'No-Hi' transition is hysteretic, as documented on *figure 5* for one sample case. A detailed investigation of this subcritical bifurcation was however not carried out.

While the representation of results in *figure 4* as a function of Re_D is well adapted for the identification of the 'No-Hi' transition thanks to abrupt jumps of St_D and amplitude, characteristic of a subcritical bifurcation, the transition 'Hi-Lo' is difficult to see. The latter appears much clearer in a plot of peak spectral power versus disc distance s. Rather than replotting our present data, we prefer to show here the original result of Monkewitz and Fernholz [16] as *figure 6*.
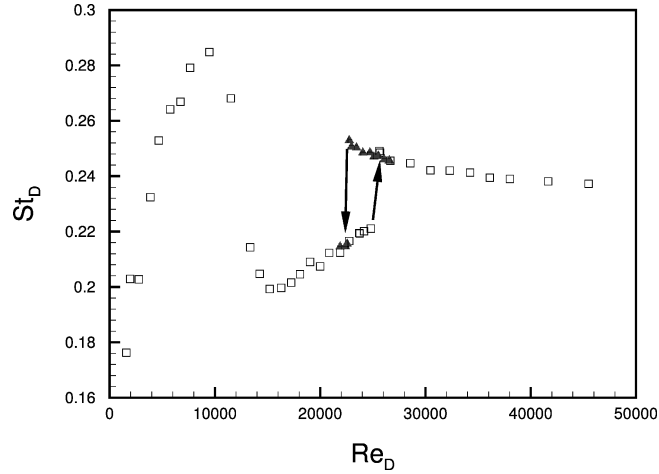
Figure 5. Strouhal number versus Re_D for $s = 0.3$. $\square$, increasing Re_D; $\blacktriangle$, decreasing Re_D.
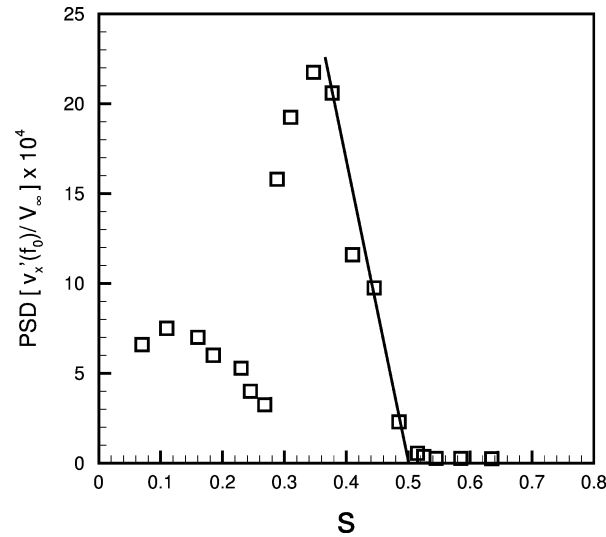

Figure 6. Peak spectral power density of the longitudinal velocity fluctuations at the fundamental frequency f_0 measured at $x/D = 2.6$ and $r/D = 0.38$ versus s for $Re_D = 2.43 \times 10^4$ (from Monkewitz and Fernholz [16]).

From this *figure 6* it is immediately apparent that the transition 'Hi-Lo' has a different character than the hysteretic 'No-Hi' transition. The linear decrease of power, i.e. amplitude squared, towards $s = 0.5$ (indicated by the solid line in *figure 6*) strongly suggests that this transition is indeed a Hopf bifurcation at $s_{\text{crit}}(Re_D = 2.43 \times 10^4) = 0.5$,[3] analogous to the onset of Kármán shedding behind a cylinder (see, e.g., Provansal et al. [18] or Schumm et al. [4]). This also allows us to characterize the vortex shedding in the 'Hi'-regime as self-excited.

Finally, the geometry of the shed vortices has also been investigated in our setup. Consistent with the well-known fact that the preferred instability mode in the axi-symmetric wake is a simple spiral (see, e.g., Monkewitz

---

[3] This $s_{\text{crit}} = 0.5$ is somewhat higher than the s_{crit} of the present study for the same Re_D (cf. *figure 3*) since no boundary trip was used in [16].
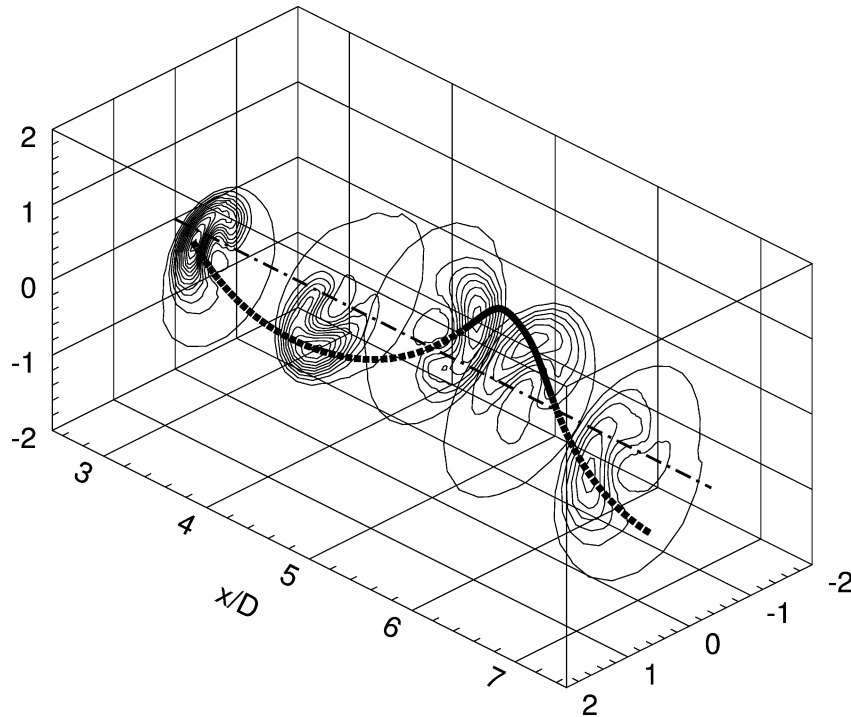
Figure 7. Downstream evolution of the phase-locked velocity $\langle V_x \rangle / V_\infty \in [0.75, \ldots, 0.99]$ in steps of 0.02 for $Re_D = 3 \times 10^4$ and $s = 0.32$.

[24] and the experimental observations of Berger et al. [10]) and, more specifically, with the findings of Monkewitz and Fernholz [16] for the Mair-body, the spiral nature of the large-scale vortex structure in the wake has been confirmed by phase-locked measurements of the instantaneous streamwise velocity field $\langle V_x \rangle (x, r)$. The phase reference was thereby provided by a single fixed hot-wire at $x/D = 6$, $r/D = 0.7$ and $\theta = 75°$ mounted through the tunnel wall in a manner which did not perturb the wake. The result of this LDA survey is displayed in *figure 7* which shows graphically that the instantaneous velocity minima at different x/D are located on a spiral which precesses around the axis at the nondimensional rate St_D. The off-axis displacement of the wake center, corresponding to the velocity minima in *figure 7*, is thought to be due to the transverse velocity field of a strong spiral vortex parallel to the spiral connecting the velocity minima, but the streamwise vorticity best suited to locate this vortex could not be measured with sufficient accuracy in our setup. The precession of the axial velocity minimum around the axis at any fixed x-position in the near wake now also explains the observation of the 'W-shaped' mean velocity profiles in the regime 'Hi' (see *figure 2*).

4. The Mechanism leading to the high and low drag regimes

In this section, an attempt is made to develop a better understanding of the fluid mechanics underlying the transitions between regimes, in particular between the 'No', 'Hi' and 'Lo' regimes. The present investigation is thereby building on earlier conjectures and measurements, primarily Mair's [13] pressure measurements, his concluding remark

"... The only possible mechanism of unsteady flow seems to be a 'breathing' of the cavity, associated with an inward and outward movement of the shear layer ..."

and the suggestive flow visualizations and mean velocity measurements of Little and Whipkey [14] in and around the cavity. These studies, together with the considerations of section 3.2, make it clear that the key to a better understanding of the drag variations is the detailed knowledge of the flow in the near wake and around the control disc. The next step is therefore to complement the above mentioned studies by steady and, more importantly, unsteady flow measurements which are presented in the following section 4.1.

4.1. Flow survey in the near wake and around the control disc

First, the mean axial centerline velocity V_x $(r = 0)$ downstream of the control disc has been measured by LDA for a fixed Re_D and four control disc positions s. The result, shown in *figure 8*, reveals that for all s, except for $s = 0.32$ in the 'Hi'-regime, recirculation exists to different degrees with a free stagnation point at the same location (measured from the cylinder base!) as without control disc (cf. *table IV*). Even more surprisingly, no reverse flow in the mean is found in the high drag regime with $s = 0.32$, and the mean axial velocity on the centerline is everywhere significantly higher than in the other regimes. This finding is likely related to the 'W -shaped' mean profiles (cf. *figure 2*) in this regime, but it is at present not clear whether this is a sufficient explanation for the complete disappearance of mean reverse flow on the centerline.

Second, a survey of the mean axial flow with a better spatial resolution than in Little and Whipkey [14], in particular in the immediate vicinity of the disc edge, appeared necessary. The mean axial velocity profiles V_x $(x/D = s, r/D)$ in the plane of the control disc, determined by LDA, are shown in *figure 9* for $Re_D = 3 \times 10^4$ and four representative control disc positions covering the regimes 'No' to 'Lo'. In the regime 'No' $(s = 0.2$ and 0.27), *figure 9* clearly shows a layer of mean reverse flow over the edge of the disc, which becomes thinner as s is increased. Remarkably, the flow rate into the cavity obtained from these profiles is approximately the same for both control disc positions.

The velocity profiles in the 'Hi' $(s = 0.32)$ and 'Lo' $(s = 0.5)$ regimes, on the other hand, show no reverse flow in the mean and are very similar between themselves. Compared to the profiles in the 'No'-regime, they have a smaller maximum radial gradient even though the point where $V_x/V_\infty = 0.5$ is closer to the disc edge located at $r/D = 0.4$. Since the unsteadiness of the wake is small in the 'Lo'-regime $(s = 0.5)$, one can
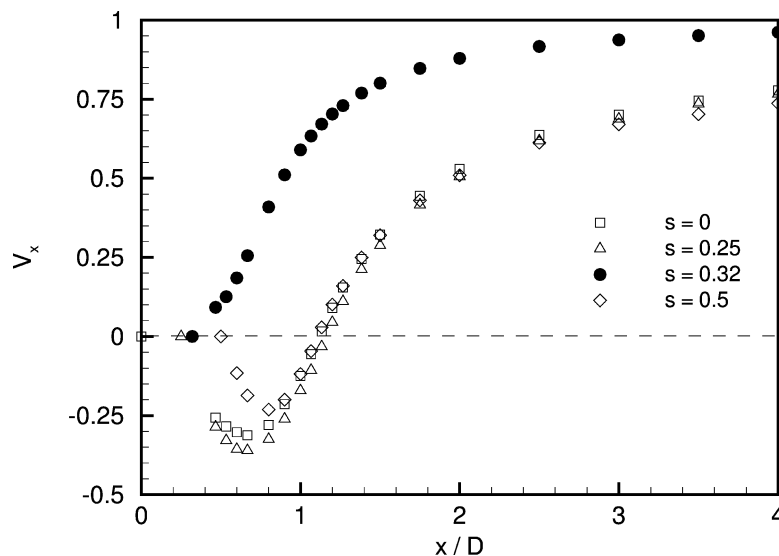

Figure 8. Normalized mean axial velocity on the centerline for $Re_D = 3 \times 10^4$ and different disc positions s.
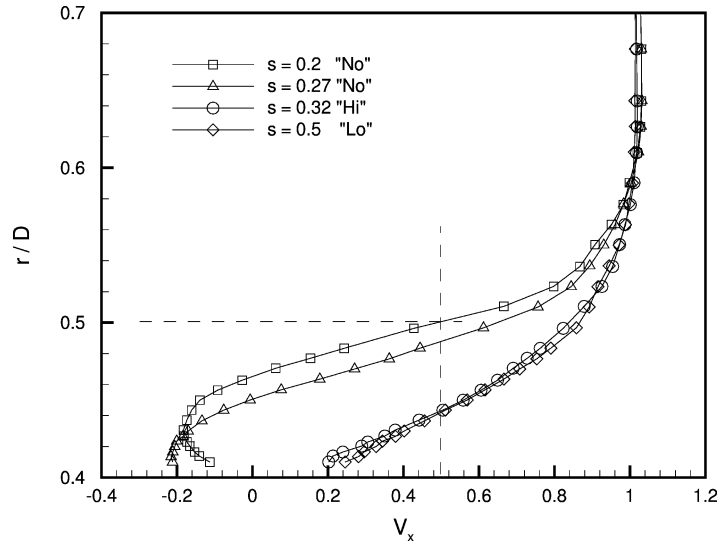
Figure 9. Normalized mean axial velocity profiles above the control disc edge for different disc positions s.

conclude that in this regime there is no back flow over the disc edge into the cavity at any instant, in agreement with Little and Whipkey's [14] measurements. In the 'Hi'-regime ($s = 0.32$), on the other hand, the mean profile does not yield much information (Little and Whipkey's data are also inconclusive in this regime) and an investigation of the instantaneous flow field is necessary.

Since the flow phenomena in the high drag regime at $s = 0.32$ are clearly periodic, the time evolution of the velocity field is best obtained by phase averaging with respect to a fixed reference probe. The components V_x and V_r along a radius in the disc plane $x/D = s$ were obtained by LDA and data were processed by sorting them into 24 phase-bins of size $\Delta\Phi = \pi/12$. *Figure 10* shows at the same time iso-contours of the phase-averaged axial velocity $\langle V_x \rangle (x/D = s, r/D)$ and the projection of the velocity vector onto the (x, r)-plane over a full oscillation period.

The iso-contours of phase-averaged axial velocity in *figure 10* clearly reveal reverse flow over the disc edge for phases Φ between 250° and 370°, i.e. over approximately a quarter of a period. The maximum flow rate into the cavity, found at $\Phi = 315°$, is however only about one quarter the steady flow rate in the 'No'-regime (cf. *figure 9*). From the shape of an intermediate iso-contour (e.g., $\langle V_x \rangle = 0.5$) it is seen that the shear layer surrounding the disc is indeed flapping in and out in an approximately sinusoidal manner. Furthermore, the high positive velocity very close to the disc edge during the closest shear layer approach at around $\Phi = 90°$ implies that a sizeable part of the low-velocity part of the shear layer is peeled off by the disc and recirculated into the cavity.

This picture of the unsteady flow field in the 'Hi'-regime is now completed by the flow visualizations of *figure 11* showing the trailing edge of the Mair-body and the control disc in side view. Six thin carbon fiber streamers, located in a common (x, r)-plane and numbered (1) to (6), are visible together with the reference hot-wire in the top right corner. Two of the streamers are located in the shear layer on opposite sides of the cylinder and are identified by arrows. Due to their flexibility they tend to align themselves with the local instantaneous flow direction. Four additional filaments are attached symmetrically on both faces of the control disc in such a manner that their rest positions are against the disc face, pointing radially outwards. In the regime 'Hi', the strong oscillations of the streamers require the use of a stroboscope to freeze their rapid motion. In *figure 11* only two phases, separated by half a fundamental period and identified as (a) and (b), are shown.
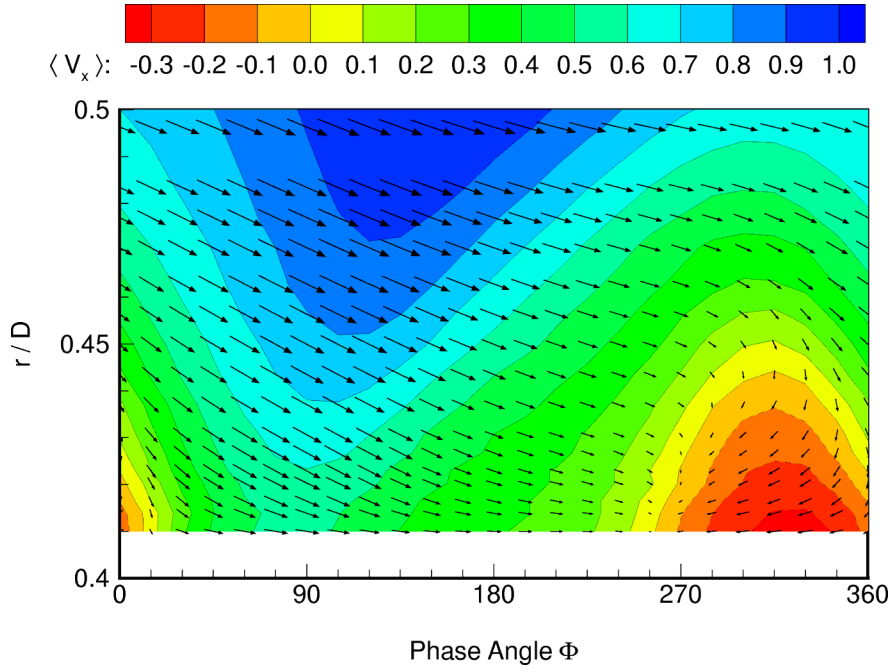
Figure 10. Phase-averaged velocity as a function of r/D and phase angle Φ for $Re_D = 3 \times 10^4$ and $s = 0.32$. Iso-contours of $\langle V_x \rangle / V_\infty$ in color and velocity vectors ($\langle V_x \rangle$, $\langle V_r \rangle$) drawn as arrows (the edge of the control disc is located at $r/D = 0.4$). Reference hot wire located at $x/D = 6$, $r/D = 0.7$ and $\theta = 75°$.
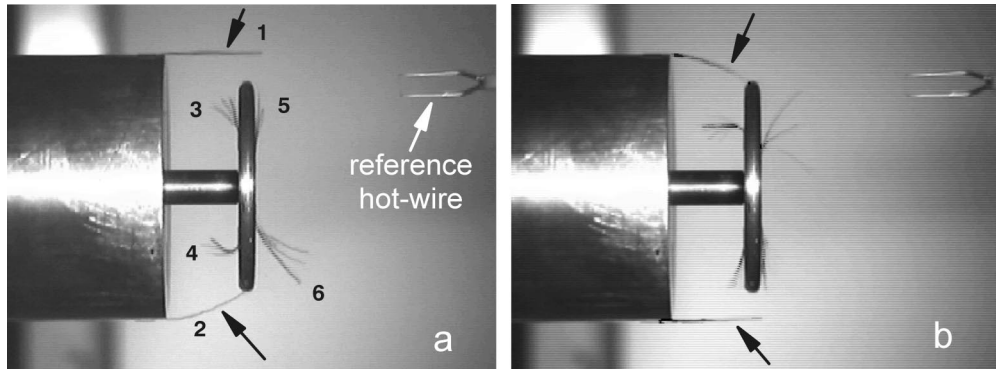

Figure 11. Visualization of the free shear layer and the flow around the disc by carbon fiber streamers at $Re_D = 3 \times 10^4$ and $s = 0.3$ (side view); phase difference between (a) and (b) is $\Delta\Phi = \pi$.

In the snapshot of *figure 11(a)* the upper fiber (1) is parallel to the cylinder, indicating that the shear layer leaving the cylinder there is straight and parallel to the x-axis, while fiber (2) on the opposite side is maximally curved towards the axis (it's end actually touches the edge of the disc). Half a period later in *figure 11(b)* the roles of these two fibers are interchanged. Hence we can identify the instant at which fiber (1) is straight in *figure 11(a)* with the phase $\Phi \approx 315°$ of the largest distance of the shear layer from the disc edge in *figure 10*. Conversely, the instant where fiber (1) has maximum curvature in *figure 11(b)* corresponds to $\Phi \approx 135°$. This leads to the conclusion, that the 'open' and 'closed' flow states are precessing in the θ-direction with angular

velocity $\dot{\Phi} = 2\pi f_0$. In other words, *figure 10* obtained for a fixed $\theta = \theta_0$ can be used for any θ, provided Φ is replaced by $\Phi \pm (\theta - \theta_0)$, with the sign depending on the sense of rotation. [4]

The behaviour of the fibers attached to the disc further confirm the deductions from *figure 10*: in *figure 11(a)*, the fiber (3) on the upper inside face of the disc is slightly bent, showing flow towards the axis, while the corresponding fiber (5) on the downstream side is stuck against the face. This corroborates the finding that some fluid flows over the disc edge into the cavity during the part of the cycle where the shear layer is furthest away from the disc edge. During the part of the cycle where the shear layer is closest to the disc edge (e.g., fiber (2) in *figure 11(a)*, on the other hand, both fibers (4) and (6) are strongly bent. Fiber (4) confirms that at this phase the inner part of the shear layer is peeled off by the disc and flows along the upstream disc face towards the axis, while fiber (6) indicates a similarly strong flow on the downstream face. This latter flow towards the axis is entirely consistent with our finding that in the regime 'Hi' no mean reverse flow exists on the axis downstream of the disc (cf. *figure 8*).

4.2. Synopsis of the observed flow phenomena

In the following, the results of this and previous studies are integrated into a qualitative description of the flow phenomena characterizing the different drag regimes. It is evident from the measurements above the control disc edge and the flow visualization of section 3.2 that the free shear layer or mixing layer between the trailing edge of the cylinder and the control disc plays a key role, in particular its thickness and entrainment rate (cf. section 3.2). This free shear layer entrains fluid both from the inside and the outside. The fluid entrained on the inside must of course be replaced. Without disc this happens by reverse flow in the separation bubble supplied from the free stagnation point region. With control disc, the situation is more complex as the recirculation zone is divided into two parts, the cavity and a part downstream of the disc. The different drag regimes are now distinguished by the way the mass entrained from the cavity is replaced The three replacement modes, corresponding to the regimes 'No', 'Hi' and 'Lo', are illustrated in *figure 12* by 'cartoons'.

In the regime 'No', i.e. for small s, the annular gap between the inwardly curved mixing layer originating from the cylinder trailing edge and the disc edge leaves a sufficiently large passage for the complete replacement of entrained fluid (solid arrow in figure *figure 12*, top) by reverse flow into the cavity (open arrow). This reverse flow over the disc edge is axisymmetric and essentially steady, so that the disc in regime 'No' can be considered as a mere obstruction in the no-disc recirculation bubble [5] with little effect on the drag. This steady reverse flow is consistent with the pressure measurements of Mair [13] who found a smaller pressure in the cavity than on the downstream face of the disc and the negligible effect on the drag suggests that the resulting 'propulsive' pressure force compensates the increased pressure drag of the cylinder.

As s is increased, the point is reached where the gap between the thickening inwardly curved mixing layer and the disc edge becomes so small that the reverse flow replacing the entrainment from the cavity is choked off. As a consequence, the cavity pressure drops and the mixing layer is sucked further towards the axis. If the flow remained steady, one would expect the mixing layer to be drawn inwards in an axisymmetric fashion until a sufficient portion of it is peeled off by the disc and diverted back into the cavity to exactly replace the entrained fluid. This 'short circuit' mode for the replacement of cavity fluid is actually the one found by Mair

---

[4] The sense of rotation depended on random perturbations during the startup of the wind tunnel and could be changed by a deliberate strong perturbation during the course of an experimental run. Statistically, both directions of rotation were found to occur with equal probability.

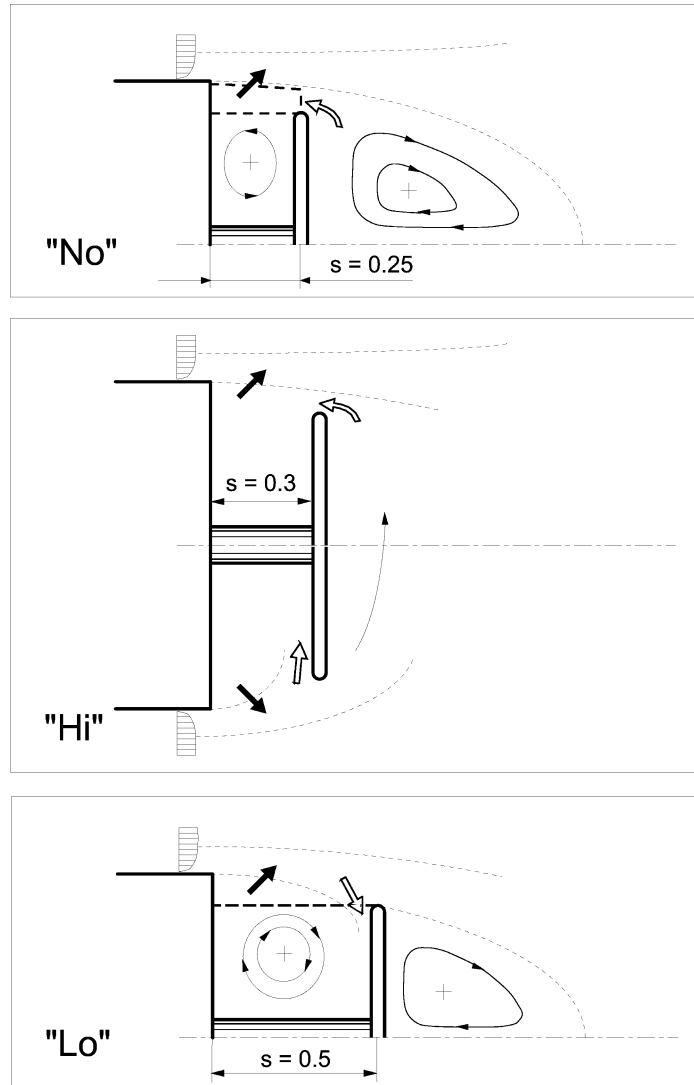[5] As shown in section 4.1, the free stagnation point does not move.

Figure 12. Sketch of flow patterns for the regimes 'No', 'Hi' (saturated state) and 'Lo'. Closed arrows: entrained fluid; Open arrows: replacement of cavity fluid; . . . : boundary of the mixing layer; − − − : control volume or surface used to analyze the stability of the 'No' and 'Lo' regimes.

[13] in the regime 'Lo', shown in *figure 12*, bottom. The mixing layer impinging on the disc edge must also alter pressures in the cavity and on the downstream face of the disc which lead to the observed net drag reduction. [6]

The regime 'Hi', finally, can be regarded as an intermediate regime in which the system cannot 'decide' between the 'No' and the 'Lo' modes of cavity fluid replacement. As documented earlier, it is an inherently unsteady regime in which a region of reverse flow over the disc edge and a region of partial shear layer impingement on the disc precess around the disc when the oscillations are saturated (cf. *figure 12*, middle). This mode must result from an non-axisymmetric instability of the axisymmetric base flow, which will be

---

[6] Mair's [13] pressure measurements are too sparse to make a sufficiently complete comparison of pressure distributions in the 'No' and 'Lo' regimes. It is however curious to note that his 35 % maximum drag reduction relative to the no-disc case is essentially equal to the 36 % area reduction of the control disc relative to the cylinder base, as if the no-disc base pressure was simply transferred to the smaller control disc.

the subject of the following section 4.3. It also appears that this self-excited instability (cf. section 3.3) is an instability of the cavity flow and that the associated strong spiral vortex shedding in the wake is just the result of the strong forcing by the cavity oscillations.

4.3. Linear stability considerations relating to the onset of flow oscillations in the high drag regime

Before attempting to model the observed cavity instability in the high drag regime, it is useful to eliminate two possible explanations on the basis of the observed oscillation frequencies. The first is an acoustic cavity oscillation, already excluded by Mair [13], for which the lowest Strouhal number corresponding to an axisymmetric mode is readily estimated for our range of Re_D as

$$St_{D,\text{acoust}} = \frac{3.832}{\pi M_\infty} \gtrsim 25, \tag{5}$$

where 3.832 is the first zero of the Bessel function J_1 and M_∞ is the free stream Mach number. Secondly, one can exclude the Kelvin–Helmholtz instability of the mixing layer surrounding the cavity as responsible for the observed cavity oscillations. The frequency of a saturated K-H mode is well approximated by the linear neutral frequency (see, e.g., Monkewitz and Huerre [25]) and can hence be estimated as follows:

$$St_{D,K-H} = (\pi \delta_\omega / D)^{-1} \frac{V_{\max} + V_{\min}}{2 V_\infty}, \tag{6}$$

where δ_ω is the vorticity thickness. The lowest K-H frequency relevant to the cavity oscillation is therefore determined by the largest thickness at the disk location $x/D = s$. From *figure 9* we find, for $s = 0.27$, $\delta_\omega(x/D = s) \approx 0.09D$ and a nondimensional average velocity of approximately 0.4. With these values, the minimum passage frequency of K-H billows at $x/D = s$ is $St_{D,K-H} \approx 1.4$, considerably larger than the observed cavity oscillation frequency. Hence, we conclude that the K-H instability plays no role in the cavity oscillations under investigation. The mechanism leading to self-excited oscillations in the cavity of the Mair-body must therefore, despite the geometric similarities, be completely different from the one identified by Gharib and Roshko [26] in a ring cavity where K-H waves on the shear layer are an essential link in the feedback loop.

Having ruled out the above two mechanisms, we attempt a linear stability analysis of the system by (crudely) modelling the dynamics of each of its components and matching them by a control volume or surface approach. In the following, all variables are made nondimensional with D and V_∞ (pressure with ρV_∞^2) and we start by analyzing the cavity modes in the region $x \in [0, s]$ and $r \lesssim d/2$, in which the time-averaged velocity is approximated by zero and the perturbation field is assumed to be x-independent. Solutions of the continuity and the linearized incompressible Euler equations are sought in normal mode form, where all perturbation quantities q' are written as $q' = \hat{q}(r)e^{im\theta - i\omega t}$ with m the azimuthal wave number and ω the (complex) frequency. Starting with the mode $m = 0$, it is clear that all axisymmetric solutions are singular on the axis. For the mode $m = 1$, the non-singular solution corresponds to an 'orbital' solid-body motion of the cavity fluid and is given by

$$
\begin{aligned}
v_r' &= \hat{v}_c e^{i\theta - i\omega t}, \\
v_\theta' &= i\hat{v}_c e^{i\theta - i\omega t}, \\
p' &= i\omega r \hat{v}_c e^{i\theta - i\omega t}.
\end{aligned}
\tag{7}
$$

Since $m = 1$ is the experimentally observed azimuthal wave number, the analysis is restricted in the following to this $m = 1$ mode.

4.3.1. Analysis of the 'No-Hi' transition

For the analysis of the 'No-Hi' transition, where the base flow includes a ring region of reverse flow around the disc edge, the conservation of mass in integral form is best formulated for a control volume bounded by $x = 0$, $x = s$, $\theta = const.$, $\theta + d\theta = const.$, $r = d/2$ (d being the disc diameter), and $r = r_0(x)$, where we have introduced the radius r_0 at which the mean axial velocity is zero (see *figure 12*, top). The downstream face of this volume, between $r = d/2$ and $r = r_0(s)$, thus corresponds to the region of mean reverse flow through the plane $x = s$. To fix ideas, r_0 and its perturbation r_0' are assumed to have the simple parabolic form

$$r_0 + r_0' = \frac{1}{2} - \frac{x^2}{s^2}(\Delta_s + \Delta_s'); \quad \Delta_s' \equiv \hat{\Delta}_s e^{i\theta - i\omega t}, \tag{8}$$

where Δ_s characterizes the mean inward deflection of the mixing layer at $x = s$ and $\hat{\Delta}_s$ is the corresponding flapping amplitude.

Proceeding now to the determination of the volumetric flow rate out of the control volume across its different faces, the contribution of the inner surface $r = d/2$ is readily evaluated from equation (7):

$$d\hat{Q}_{\text{in}} = -s(d/2)\hat{v}_c d\theta. \tag{9}$$

The net contribution of the two lateral faces is also easily estimated as $dQ_{\text{lat}}' = s(\bar{r}_0 - d/2)(\partial v_\theta'/\partial\theta)d\theta$, where the overbar denotes an x-average over the interval $[0, s]$. With v_θ' from equation (7), one obtains

$$d\hat{Q}_{\text{lat}} = -s(\bar{r}_0 - d/2)\hat{v}_c d\theta. \tag{10}$$

Next, we turn to the mixing layer around the cavity. As argued in section 3.2, the entrainment from the cavity plays an important role. It is a fraction of the total entrainment which is proportional to the x-derivative of the mixing layer thickness $\delta(x)$, provided the velocity profiles are self-similar. While this condition is approximately satisfied in the steady case (for straight mixing layers see, e.g., Dimotakis [22]; mixing layers with streamwise curvature have, to our knowledge, only been studied by Wang [27]), little is known about the unsteady entrainment of flapping mixing layers. Therefore, the radial entrainment velocity perturbation relative to the moving inner boundary of the mixing layer $r = r_0 + r_0'$ (cf. equation (8)) is modelled as

$$\hat{v}_{r,\text{relent}} = \alpha \frac{\hat{\Delta}_s}{s}, \tag{11}$$

where $\hat{\Delta}_s/s$ is the x-average of the spreading rate perturbation $(d\delta/dx)' \approx -dr_0'/dx$, analogous to the spreading rate appearing in the expression for the mean entrainment velocity, and α is a proportionality factor to be fitted. Since $\hat{v}_{r,\text{ent}}$ is the entrainment velocity perturbation relative to the moving surface $r = r_0 + r_0'$, the entrainment perturbation velocity at, say, the fixed $r = \bar{r}_0$ is given by

$$\hat{v}_{r,\text{ent}} = \left(\frac{\alpha}{s} - \frac{1}{3}i\omega\right)\hat{\Delta}_s. \tag{12}$$

The second term of equation (12) represents $\partial r_0'/\partial t$ obtained from equation (8), averaged over the cavity length. With the above result (12), the contribution of the outer control surface $r = \bar{r}_0$ to the volumetric flow rate out of the control volume becomes

$$d\hat{Q}_{\text{out}} = s\bar{r}_0\left(\frac{\alpha}{s} - \frac{1}{3}i\omega\right)\hat{\Delta}_s\,d\theta. \tag{13}$$

To complete the analysis of the mixing layer, one has to relate the perturbation of the mixing layer deflection $\hat{\Delta}_s$ to the pressure perturbation $\hat{p}_0$ on the inside $r = \bar{r}_0$ of the mixing layer. For this, the principal terms in the equation for the radial momentum perturbation

$$\frac{\partial v_r'}{\partial t} - \left(\frac{V_x^2}{R_{sc}}\right)' \approx -\frac{\partial p'}{\partial r}, \tag{14}$$

need to be estimated, where R_{sc} is the radius of streamwise curvature. Omitting the factor $e^{i\theta-i\omega t}$, the first term of equation (14) is modelled as $+\omega^2\hat{\Delta}_s$.[7] To linearize the second term, the radius of curvature is approximated by $R_{sc}^{-1} \approx 2s^{-2}(\Delta_s + \Delta_s')$ and the axial velocity relevant to the centripetal acceleration is estimated as $V_x \approx V_{sc} + (\Delta_s'/\bar{\delta})$, with $\bar{\delta}^{-1}$ the nondimensional radial velocity gradient at the radius where $V_x = V_{sc}$.[8] The right-hand side of equation (14) is approximated by $+p_0'/\bar{\delta}$ [9] which leads to the result

$$\hat{p}_0 = (\omega^2 - C_{ml})\bar{\delta}\hat{\Delta}_s \quad \text{with } C_{ml} \equiv \frac{2V_{sc}}{s^2}\left(\frac{2\Delta_s}{\bar{\delta}} + V_{sc}\right). \tag{15}$$

The perturbation of the reverse flow rate through the end face, finally, is given by

$$dQ_{\text{rev}}' = -\left(V_{\text{rev}}dS_{\text{end}}' + v_{\text{rev}}'dS_{\text{end}}\right), \tag{16}$$

where $V_{\text{rev}} > 0$ is taken to point into the control volume, and the end surface area is given by

$$dS_{\text{end}} + dS_{\text{end}}' = \left[C_e - \left(\frac{1}{2} - \Delta_s\right)\Delta_s'\right]d\theta \quad \text{with } C_e \equiv \frac{1}{2}\left[\left(\frac{1}{2} - \Delta_s\right)^2 - \frac{d^2}{4}\right]. \tag{17}$$

The velocity perturbation v_{rev}' is obtained from the unsteady Bernoulli equation, applied between a stagnation point downstream of the disc and the end face of the control volume. Modelling the unsteady term $\int(\partial\vec{v}'/\partial t)\cdot d\vec{l}$ by $-i\omega\,\hat{v}_{\text{rev}}\,l_{\text{acc}}\,e^{i\theta-i\omega t}$, with l_{acc} to be fitted, one has

$$\hat{v}_{\text{rev}} = -\hat{p}_0(V_{\text{rev}} - i\omega l_{\text{acc}})^{-1}. \tag{18}$$

Combining equations (16), (17) and (18), one finally obtains for the contribution of the end surface to the volumetric flow rate perturbation

---

[7] The sign is positive because $\Delta_s' > 0$ corresponds to a deflection in the negative r-direction.

[8] During unsteady flapping, it is expected that stretching and compression of the velocity profile occurs mostly on the low-velocity side of the mixing layer. Therefore, we expect that V_{sc} will be considerably smaller than unity and that the local gradient $\bar{\delta}^{-1}$ is also smaller than δ_ω^{-1}.

[9] The sign is positive because $p_0' \equiv \hat{p}_0 e^{i\theta-i\omega t}$ is the pressure perturbation on the inside of the mixing layer.

$$d\hat{Q}_{\text{end}} = \left[V_{\text{rev}}\left(\frac{1}{2} - \Delta_s\right)\hat{\Delta}_s + C_e\hat{p}_0(V_{\text{rev}} - i\omega l_{\text{acc}})^{-1}\right]d\theta. \tag{19}$$

Since the term involving l_{acc} has been found to be non-essential, i.e. to not alter the character of the eigenvalue relation for ω, we set in the following $l_{\text{acc}} = 0$ in order to simplify the algebra. Identifying now the cavity pressure amplitude at $r = \bar{r}_0$ (equation (8)) with the pressure amplitude $\hat{p}_0$ of equation (15), i.e. $\hat{p}_0 = i\omega\bar{r}_0\hat{v}_c$, and summing the $d\hat{Q}$'s (equations (9), (10), (13) and (19)) to zero, finally leads after some algebra to the eigenvalue relation

$$i\omega^3 C_e\bar{\delta} + \omega^2 s\left(\frac{1}{3}\bar{r}_0 - \bar{\delta}\right)V_{\text{rev}} + i\omega\left[\left(\frac{1}{2} - \Delta_s\right)V_{\text{rev}}^2 + \alpha\bar{r}_0 V_{\text{rev}} - C_e C_{ml}\bar{\delta}\right] + C_{ml}s\bar{\delta}V_{\text{rev}} = 0, \tag{20}$$

with the s-dependent coefficients C_{ml} and C_e defined in equations 15 and 17, respectively. We first note that the above eigenvalue relation has the right form in the sense that the growth rate ω_i is independent of the sign of the real frequency ω_r, i.e. of the sense of precession of the perturbation. To find the point of marginal stability, the parameters in equation (20) need to be estimated. From *figure 9* we find at $s = 0.27$ $\Delta_s = 0.05$ and hence $\bar{r}_0 = 0.483$ and the average $V_{\text{rev}} \approx 0.1$. Furthermore, guided by the expectation that V_{sc} in equation (15) is small, we set somewhat arbitrarily $V_{sc} = 0.1$. The remaining two parameters α and $\bar{\delta}$, which we reasonably assume to be proportional to s, i.e.

$$\bar{\delta} = \beta s, \tag{21}$$

are now determined from equation (20) by requiring the solution ω to be neutral (real) at the Strouhal number $St_D = 0.2$ and $s = 0.3$. This yields $\alpha \approx -0.2$ and $\beta \approx 1.1$ in equation (21). The negative value of α, corresponding to a reduction of the relative velocity of entrainment from the inside as the mixing layer flaps inwards, is significant since $\alpha < 0$ is a necessary condition for the existence of a neutral solution of equation (20) if all other parameters are within reasonable physical limits. The fitted value of β, which was used to estimate the radial velocity and pressure gradients in the mixing layer, indeed appears to be within these limits. Hence there is some hope that the present model captures the essential physics. However, to use it for calculating growth rates as s is increased beyond the critical s_{No-Hi}, the s-dependence of too many parameters in the dispersion relation (20) are unknown and the exercise degenerates to arbitrary parameter fitting. Some confidence in equation (20) can however be gained by analyzing the stability of the base flow in the 'Lo' regime, in which the mixing layer is partially peeled off by the disc.

4.3.2. Analysis of the 'Lo-Hi' transition

The stability analysis of the base flow in the 'Lo' regime is simpler as it is sufficient to consider the continuity of volumetric flow rate across the control surface of area $s(d/2)d\theta$ located at $r = d/2$ (see *figure 12*, bottom). From the previous analysis, we can directly use $d\hat{Q}_{\text{in}}$, given by equation (9), and a trivially modified $d\hat{Q}_{\text{out}}$ (equation (13)) in which $\bar{r}_0$ is replaced (approximated) by $(d/2)$. Since the control surface has no lateral faces, the only additional task is the replacement of the contribution from reverse flow which no longer exists (at infinitesimal amplitude!) by the contribution from the peeled off mixing layer fluid. This contribution (counted positive if directed towards the centerline) is easily estimated as

$$d\hat{Q}_{\text{shav}} = \frac{d}{2}V_{\text{shav}}\hat{\Delta}_s d\theta, \tag{22}$$

where V_{shav} is the mean axial velocity immediately above the disc edge, i.e. $V_{\text{shav}} = V_x$ $(x = s, r = d/2 + 0)$ (the notation $r = d/2 + 0$ signifies 'just outside the very thin boundary layer on the rounded disc edge'). From *figure 9* this velocity is estimated as $V_{\text{shav}} \approx 0.2$ for $s = 0.5$.

Finally, the radial motion of the mixing layer needs to be related to the perturbation pressure on its inside. This is conveniently carried out in two steps. First, the perturbation of the stagnation pressure in the upstream vicinity of the disc edge is evaluated with the linearized Bernoulli equation, applied along the stagnation streamline between $x = 0$ and $x = s$, with the result

$$\hat{p}_{\text{stag}} = 2V_{\text{shav}}\hat{v}_{\text{shav}} = 2V_{\text{shav}}\frac{\partial V_x}{\partial r}(s, d/2 + 0)\hat{\Delta}_s. \tag{23}$$

This perturbation of the stagnation pressure is of course only felt in a neighborhood l_{stag} of the disc edge and, in order to identify it with the x-independent perturbation of the cavity pressure at $r = d/2$ (equation (7)), it needs to be smeared over the x-interval $[0, s]$, i.e.

$$i\omega\frac{d}{2}\hat{v}_c = \frac{l_{\text{stag}}}{s}\hat{p}_{\text{stag}}. \tag{24}$$

Combining equations (23) and (24) to provide a relation between $\hat{v}_c$ and $\hat{\Delta}_s$ and balancing the volumetric flow rates across the control surface yields the eigenvalue relation for ω

$$\omega^2\frac{sd}{3} + i\omega\left[V_{\text{shav}} + \alpha\right] - 4\,l_{\text{stag}}V_{\text{shav}}\frac{\partial V_x}{\partial r}(s, d/2 + 0) = 0. \tag{25}$$

From the profile for $s = 0.5$ in *figure 9* the value of approximately 8 is estimated for the derivative $(\partial V_x/\partial r)$ $(x = s, r = d/2 + 0)$ in equation (25) and $\alpha = -0.2$ is kept unchanged. The remaining parameter l_{stag} is finally determined from equation (25) by requiring the solution ω to be neutral (real) at the Strouhal number $St_D = 0.25$ and $s_{Hi-Lo} = 0.4$. This yields $l_{\text{stag}} \approx 0.04$, which appears to be a reasonable value. With the assumption that $(\partial V_x/\partial r)$ $(x = s, r = d/2 + 0)$ and l_{stag} vary only slowly with s and with $\partial V_{\text{shav}}/\partial s > 0$, [10] it is also straightforward to verify that this simpler eigenvalue relation (25) yields a positive temporal growth rate ω_i for $s < s_{Hi-Lo}$, as seen in the experiment.

Finally, equation (25) permits an assessment of the influence of the disc diameter d. Since the first and the third term in equation (25) have to balance at neutral conditions (ω real) and the coefficient of the first term contains the product sd, the critical s must increase when the disc diameter is reduced, provided the third term does not vary strongly with s. Since this corresponds to the observation (see the results of Little and Whipkey [14] for $d/D = 0.75$) the latter assumption appears justified. It does however not seem possible to draw an analogous conclusion from equation (20), pertaining to the 'Lo-Hi' transition, because of its complexity. The effect of Reynolds number, on the other hand, is much more difficult to assess since the analysis itself is inviscid and viscous effects only enter through the velocity gradients of the mixing layer, i.e. $\bar{\delta}^{-1}$ in equation (20) and $(\partial V_x/\partial r)$ $(s, d/2 + 0)$ in equation (25).

Due to the parameter fitting the evidence may not appear very strong that these models actually capture the physics of the cavity instability. We believe, however, that the situation is better than it looks as the interested reader may verify that the choice of parameters, and in particular the choice of α which is common to both

---

[10] From equation (22) this is evident, since more entrained fluid needs to be replaced as s is increased.

eigenvalue relations (20) and (25), is surprisingly restricted by physical bounds on the parameters themselves and the requirement of solvability (e.g., $\omega_r^2 > 0$ for $\omega_i = 0$). Most significantly, $\alpha < 0$ (equation (12)) is in both cases a necessary condition for the existence of a neutral solution, which clearly points to the key flow feature leading to the observed self-excited oscillations in the high drag regime. The verification of this conclusion was beyond the scope of the present study, but it could and should be verified experimentally or by direct numerical simulation.

5. Outlook

Many more detailed measurements could be made of unsteady velocity fields, in particular the flapping motion of the shear layer surrounding the cavity, and of unsteady surface pressures, but we believe that the selected data presented in this paper have permitted to paint a reasonably complete picture of the flow phenomena leading to the different drag regimes. On the analytical side, the linear stability analysis of section 4.3 can certainly be refined and improved once the unsteady entrainment of a curved, flapping mixing layer is better understood. Beyond this, the modelling of the saturated cavity oscillations in the 'Hi' regime and of the hysteretic 'No-Hi' transition by nonlinear amplitude equations, such as for instance the non-linear delayed saturation model developed by Rehab et al. [28] for flows with significant recirculation, remains an open field.

Coming back to the possible technological exploitation of the 'Hi-Lo' transition for controlling entrainment, viz. mixing rate, it is clear that the Mair-body represents a viable and simple actuator. Its main inconvenience, however, is the axisymmetric shape. This not only makes the mounting of Mair-bodies in a supply duct difficult, but if, say, two species were to be mixed, a split upstream supply system would be required to produce an interface intersecting one or several Mair-bodies parallel to their axes. Therefore, tests with a two-dimensional version of the Mair-body which could serve directly as the trailing edge of a splitter plate have been carried out (cf. Weickgenannt [19]). The preliminary results are encouraging as the Kármán vortex shedding (the 2D equivalent of spiral vortex shedding) was indeed found to be significantly enhanced for certain control strip (the 2D eqivalent of the control disc) positions. However, other problems tend to arise with three-dimensional effects originating from the end conditions, such as oblique shedding (see, e.g., Williamson [29]) that cause strong spanwise flow in the cavity and destroy the control effect of the rear-mounted strip.

References

[1] Roshko A., Perspectives on bluff body aerodynamics, J. Wind Eng. Ind. Aerod. 49 (1993) 79–100.

[2] Roshko A., On the drag and shedding frequency of two-dimensional bluff bodies, NACA TN 3169, 1954.

[3] Monkewitz P.A., Wake control, in: Eckelmann H. et al. (Eds.), Bluff-Body Wakes, Dynamics and Instabilies, IUTAM Symp., Göttingen, Germany, Springer, Berlin, 1992.

[4] Schumm M., Berger E., Monkewitz P.A., Self-excited oscillations in the wake of two-dimensional bluff bodies and their control, J. Fluid Mech. 271 (1994) 17–53.

[5] Roussopoulos K., Monkewitz P.A., Nonlinear modelling of vortex shedding control in cylinder wakes, Physica D 97 (1996) 264–273.

[6] Koochesfahani M.M., Dimotakis P.E., Mixing and chemical reactions in a turbulent liquid mixing layer, J. Fluid Mech. 170 (1986) 83–112.

[7] Achenbach E., Vortex shedding from spheres, J. Fluid Mech. 62 (1974) 209–221.

[8] Taneda S., Visual observations of the flow past a sphere at Reynolds numbers between 10^4 and 10^6, J. Fluid Mech. 85 (1978) 187–192.

[9] Scholz D., Kohärente Wirbelstrukturen im Nachlauf einer ruhenden und einer schwingungserregten Kreisscheibe, Hermann-Föttinger-Institut, Technische Universität Berlin, 1986.

[10] Berger E., Scholz D., Schumm M., Coherent vortex structures in the wake of a sphere and a circular disk at rest and under forced vibrations, J. Fluid. Struct. 4 (1990) 231–257.

[11] Schwarz V., Numerische Untersuchung zur Instabilität der Nachlaufströmung eines rotationssymmetrischen Körpers mit stumpfem Heck, Universität Stuttgart, 1996.

[12] Fuchs H., Mercker E., Michel U., Large-scale coherent structures in the wake of axisymmetric bodies, J. Fluid Mech. 93 (1979) 305–387.

[13] Mair W.A., The effect of a rear-mounted disc on the drag of a blunt-based body of revolution, Aeronaut. Quarterly 16 (1965) 350–360.

[14] Little Jr. B.H., Whipkey R.R., Locked vortex afterbodies, J. Aircraft 16 (5) (1979) 296–302.

[15] Fiedler H.E., Fernholz H.H., On management and control of turbulent shear flows, Prog. Aerospace Sci. 27 (1990) 305–387.

[16] Monkewitz P.A., Fernholz H.H., Self-exited vortex shedding behind an axisymmetric bluff body and its control, B. Am Phys. Soc. 37 (8) (1992) 1811.

[17] Fernholz H.H., Management and control of turbulent shear flows, Z. Angew. Math. Mech. 73 (1993) 287–300.

[18] Provansal M., Mathis C., Boyer L., Bénard-von Kármán instability: transient and forced regimes, J. Fluid Mech. 182 (1987) 1–22.

[19] Weickgenannt A., Entrainment Control in the Bluff Body Wake: An Experimental Study, Swiss Federal Institute of Technology, Lausanne, 1999.

[20] Fernholz H.H., Finley P.J., The incompressible zero-pressure-gradient turbulent boundary layer: An assessment of the data, Prog. Aerospace Sci. 32 (1996) 245–311.

[21] Porteiro J.L.F., Przirembel C.E.G., Page R.H., Modification of subsonic wakes using boundary layer and base mass transfer, AIAA J. 21 (1983) 665–670.

[22] Dimotakis P.E., Two-dimensional shear-layer entrainment, AIAA J. 24 (1986) 1791–1796.

[23] Monkewitz P.A., The role of absolute and convective instability in predicting the behavior of fluid systems, Eur. J. Mech. B/Fluids 9 (1990) 395–413.

[24] Monkewitz P.A., A note on vortex shedding from axissymmetric bluff bodies, J. Fluid Mech. 192 (1988) 561–575.

[25] Monkewitz P.A., Huerre P., Influence of the velocity ratio on the spatial instability of mixing layers, Phys. Fluids 25 (1982) 1137–1143.

[26] Gharib M., Roshko A., The effect of flow oscillations on cavity drag, J. Fluid Mech. 177 (1987) 501–530.

[27] Wang C., The effects of curvature on turbulent mixing layers, California Institute of Technology, 1984.

[28] Rehab H., Villermaux E., Hopfinger E.J., Flow regimes of large-velocity-ratio coaxial jets, J. Fluid Mech. 345 (1997) 357–381.

[29] Williamson C.H.K., Oblique and parallel modes of vortex shedding in the wake of a circular cylinder at low Reynolds numbers, J. Fluid Mech. 206 (1989) 579–627.